coatings

MDPI

Article

Shear Behavior and Interface Damage Mechanism of Basalt FRP Bars: Experiment and Statistical Damage Constitutive Modeling

Fengjun Liu [1,*], Pengfei Zhang [1], Jinjun Guo [2] and Yanqing Wei [2]

[1] College of Civil Engineering, Henan University of Science and Technology, Luoyang 471023, China
[2] School of Intelligent Construction and Civil Engineering, Luoyang Institute of Science and Technology, Luoyang 471023, China
* Correspondence: llffjj@haust.edu.cn

Abstract

The shear behavior of basalt fiber-reinforced polymer (BFRP) bars is crucial for their applications in geotechnical reinforcement and composite structures. In this study, double-side direct shear tests were conducted to investigate the progressive failure mechanism of BFRP bars. The results reveal a three-stage process: initial matrix-dominated vertical shear, followed by fiber-bridging dominated oblique tension-shear, and finally formation of a "brush-like" fracture surface with significant residual strength. The average peak shear strength of the ten specimens was 204.04 MPa with a coefficient of variation of 7.25%, while the initial shear modulus averaged 3.37 GPa with a coefficient of variation of 11.82%. Based on statistical damage theory, a shear constitutive model incorporating fiber bridging and residual strength is established. Parameter analysis indicates that the shape parameter m governs the post-peak softening rate, while the residual strength τ_{res} essentially determines the height of the residual plateau. The model achieves a goodness-of-fit (R^2) exceeding 0.98 for most specimens, accurately describing the mechanical behavior from linear elasticity, damage-induced hardening, peak softening, to the residual stage. This study provides theoretical and experimental support for the engineering application of BFRP bars under complex stress states.

Keywords: BFRP bar; direct shear test; failure mechanism; statistical damage theory; constitutive model; fiber bridging

1. Introduction

Fiber-reinforced polymer (FRP) bars, owing to their superior properties such as high strength, light weight, and corrosion resistance, are gradually replacing traditional steel reinforcement in both strengthening and new construction within civil engineering [1]. Basalt fiber-reinforced polymer (BFRP) bars not only share these advantages but also offer benefits including abundant raw materials, relatively low cost, and good environmental compatibility, demonstrating promising application potential in bridges, marine engineering, and seismic-resistant structures [2]. Compared to glass fiber-reinforced polymer (GFRP) and carbon fiber-reinforced polymer (CFRP), BFRP exhibits a better balance between cost, mechanical performance, and environmental friendliness, making it a competitive alternative in infrastructure applications. With a density of approximately 2.0 g/cm^3, BFRP bars are about 75% lighter than traditional steel reinforcement (7.85 g/cm^3), while offering comparable tensile strength in the range of 1000–1200 MPa. This high strength-to-weight ratio

Check for updates

Academic Editors: Mayara Amario, Karoline Figueiredo and Carina Mariane Stolz

Received: 4 February 2026
Revised: 17 February 2026
Accepted: 19 February 2026
Published: 21 February 2026

Copyright: © 2026 by the authors. Licensee MDPI, Basel, Switzerland. This article is an open access article distributed under the terms and conditions of the Creative Commons Attribution (CC BY) license.

makes BFRP bars particularly advantageous for lightweight structures, seismic-resistant design, and applications where self-weight reduction is critical.

Current research has largely focused on the tensile performance of BFRP bars, which—given their excellent corrosion resistance, high strength-to-weight ratio, and electrical insulation—show great potential for replacing conventional steel in civil engineering structures exposed to harsh environments or requiring high durability [3].

In recent years, research on the shear behavior of BFRP bars has developed at multiple levels: at the structural and system level, studies have mainly examined the shear behavior of BFRP bars in concrete beams, slabs, and rock bolts, investigating the influence of reinforcement layout, incorporation of recycled aggregates, fiber-reinforced concrete composites, and durability in seawater environments on the overall shear behavior of the members [4–6]; at the interface behavior level, research has focused on the shear interaction mechanisms between the bars and concrete or rock joints [7]. These studies generally highlight that the shear response and failure modes of structural members are deeply dependent on the inherent shear mechanical properties of the reinforcement itself.

However, there remains a notable gap in the constitutive description of the shear behavior of the bars themselves. Although some studies have tested the direct shear strength of BFRP bars and examined the effects of environmental aging [8,9], a systematic experimental and theoretical characterization of the full process and multi-stage damage evolution during shear failure is still lacking. Most existing models focus on peak strength prediction without capturing the post-peak softening and residual stages, which are crucial for understanding the ductility and energy dissipation capacity of BFRP-reinforced structures. The shear failure of BFRP bars is not a simple brittle fracture but a progressive composite process involving resin matrix shear, fiber-matrix interface debonding, fiber bridging, and finally fiber pull-out. Existing design guidelines, such as those from ACI [10], often adopt over-conservative strength reduction formulas that lack mechanistic description. Meanwhile, mechanism-based models considering fiber tension-friction coupling—such as the empirical correlation between shear and tensile strengths proposed by Protchenko [11]. based on extensive testing of BFRP and hybrid FRP bars—still fail to describe the post-peak softening and residual strength plateau.

Therefore, establishing a constitutive model capable of reflecting the full-range shear behavior of BFRP bars is a critical link between material characterization and the performance prediction of structural members—and remains an underdeveloped area in current research. This study aims to fill this gap by proposing a statistical damage-based constitutive model that captures the entire shear process, including elastic, hardening, softening, and residual stages, with clear physical interpretations of each parameter. This paper conducts systematic double-sided direct shear tests to thoroughly investigate the macroscopic failure modes and microscopic damage mechanisms of BFRP bars. Building on this, a constitutive model describing the complete shear process is developed by integrating statistical damage theory. Within the classical statistical damage framework, the model incorporates influence factors related to fiber orientation angle and volume fraction, enabling the coupled representation of macroscopic shear deformation and axial fiber bridging effects [12–15]. Through systematic parameter fitting, sensitivity analysis, and model validation, the physical significance of each parameter and its influence on mechanical behavior are clarified, aiming to provide theoretical and technical support for the engineering application, performance optimization, and numerical simulation of BFRP bars.

2. Experimental Overview

2.1. Materials and Specimens

The test employed BFRP bars with a diameter of 22 mm and a fiber volume fraction of approximately 70%, using epoxy resin as the matrix material. All bars were fabricated with basalt fibers and pultruded with a twisted braid surface to enhance concrete adhesion.

To obtain statistically meaningful shear mechanical responses and to investigate the generality of the failure mechanism, a total of 10 specimens with identical geometry were prepared for repeated testing. Each specimen had a length of 200 mm to ensure the shear region was located in the middle of the bar, thereby effectively avoiding end effects. The detailed design and fundamental parameters of the specimens are summarized in Table 1.

Table 1. Mechanical performance parameters (The tensile strength and shear strength were obtained through uniaxial tensile tests and direct shear tests, respectively, following the recommendations of ACI 440.3R-12. The elastic modulus was derived from the initial linear segment of the stress–strain curve, and density was measured using the water displacement method.).

Type	Tensile Strength/MPa	Shear Strength/MPa	Elastic Modulus/GPa	Density/g·cm^{-3}
BFRP reinforcement	1031	140	45	2.03
Metal mold	700	--	210	7.85
BFRP base epoxy resin	75	--	4.0	1.25

2.2. Double Shear Test

The direct shear test on the bars was conducted using an RMT-301 rock and concrete mechanical testing system, following the general principles of ASTM D7205 for shear testing of FRP bars. A custom-made metal mold with dimensions of 100 mm × 100 mm × 100 mm was employed, capable of performing double-sided shearing on the BFRP bars.

The test was performed in displacement-controlled mode at a loading rate of 0.5 mm/s. The maximum vertical load capacity was set to 1500 kN, and the vertical displacement range was 50 mm. The testing machine automatically and continuously recorded the vertical load P and the platen displacement Δ. The test was terminated when bar fracture or internal fiber tearing occurred, accompanied by no further increase in load or displacement. A schematic diagram of the test setup is shown in Figure 1.

The experimental data were processed using Equations (1) and (2) to obtain the true shear stress (τ) versus shear strain (γ) curve of the bars [16]:

$$\tau = \frac{P}{2A} \tag{1}$$

$$\gamma = \frac{\Delta}{L} \tag{2}$$

where

P = vertical load (N);

A = cross-sectional area of the specimen (mm^2);

Δ = shear displacement (mm);

L = interface height (mm).

Since the testing machine software may potentially misinterpret readings, the application of the formulas above allows for a more accurate representation of the shear stress–strain relationship of the BFRP bars.

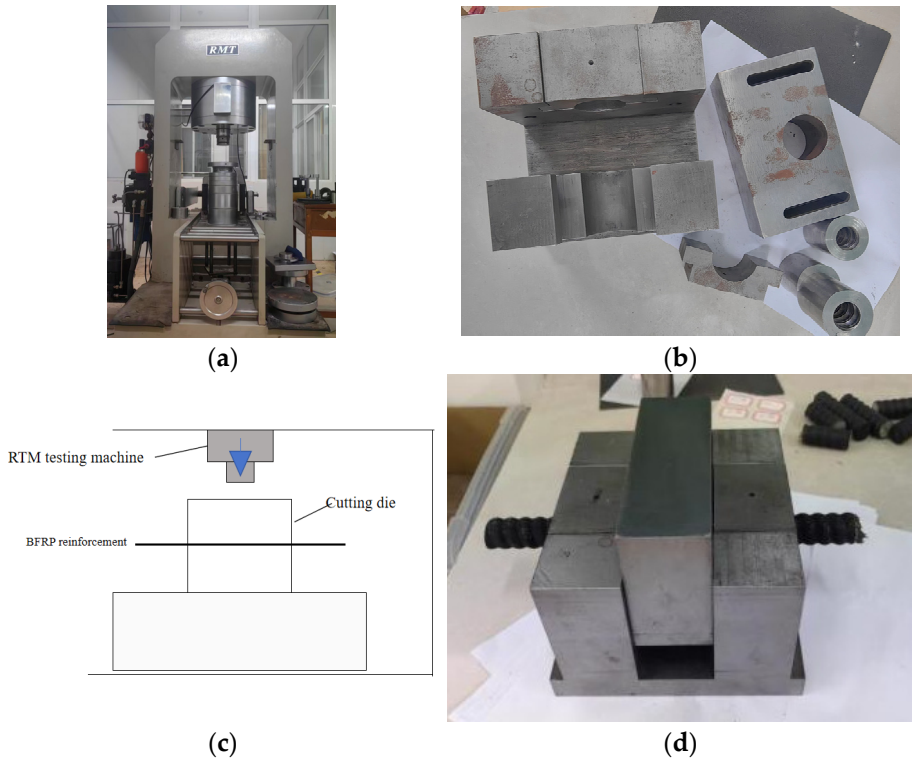

Figure 1. Photographs and schematic of the direct shear test setup. (**a**) RMT-301 rock and concrete mechanics test system; (**b**) Custom-made metal shear mold; (**c**) Diagram of the device; (**d**) Schematic diagram of the double-side shear loading configuration.

2.3. Macroscopic Fracture Surface Analysis

Following the test, a camera was used to capture the macroscopic morphology of the fracture surface of each specimen. Using ImageJ image processing software (version 1.53t), the angle between the final failure plane and the axis of the bar was measured on the photographs. This angle is defined as the fiber orientation angle θ, as shown in Figure 2. A total of 45 valid θ measurements were obtained through the software, which are treated as a statistical sample from this batch of material. Although scanning electron microscopy (SEM) was not performed in this study due to equipment limitations, the macroscopic "brush-like" fracture morphology and measured fiber angles (n = 45) provide sufficient evidence for the proposed failure mechanism.



Figure 2. Macroscopic fiber failure surface with measured inclination angle θ. This photograph was used for statistical analysis of fiber orientation (n = 45).

3. Experimental Results and Analysis

3.1. Failure Mode

Experimental observations indicate that all specimens exhibited a highly consistent and progressive failure process. The failure progresses through three distinct stages:

(1) Vertical shear stage: matrix-dominated shear along the predetermined plane, characterized by a relatively smooth fracture surface (Figure 3a).
(2) Transition stage: onset of fiber pull-out and bridging; the fracture surface becomes irregular (Figure 3b).
(3) Oblique tensile-shear stage: extensive fiber pull-out forming a "brush-like" morphology (Figure 3c,d).

Figure 3 illustrates the typical failure mode of BFRP bars under double-sided direct shear testing. In the initial loading phase, the specimen primarily experienced vertical shear at the predetermined shear plane. As the load approached its peak, a sudden lateral slippage was observed, with the fracture surface displaying a relatively smooth "shear-off" characteristic (Figure 3a). After the peak load, the failure mode fundamentally changed. The two separated segments of the bar did not fully detach; instead, a large number of basalt fibers were pulled out, stretched, and noticeably inclined at the fracture surface, forming a "brush-like" morphology (Figure 3b,c). This phenomenon indicates that the failure mechanism transitioned to oblique tensile failure dominated by fiber bridging.

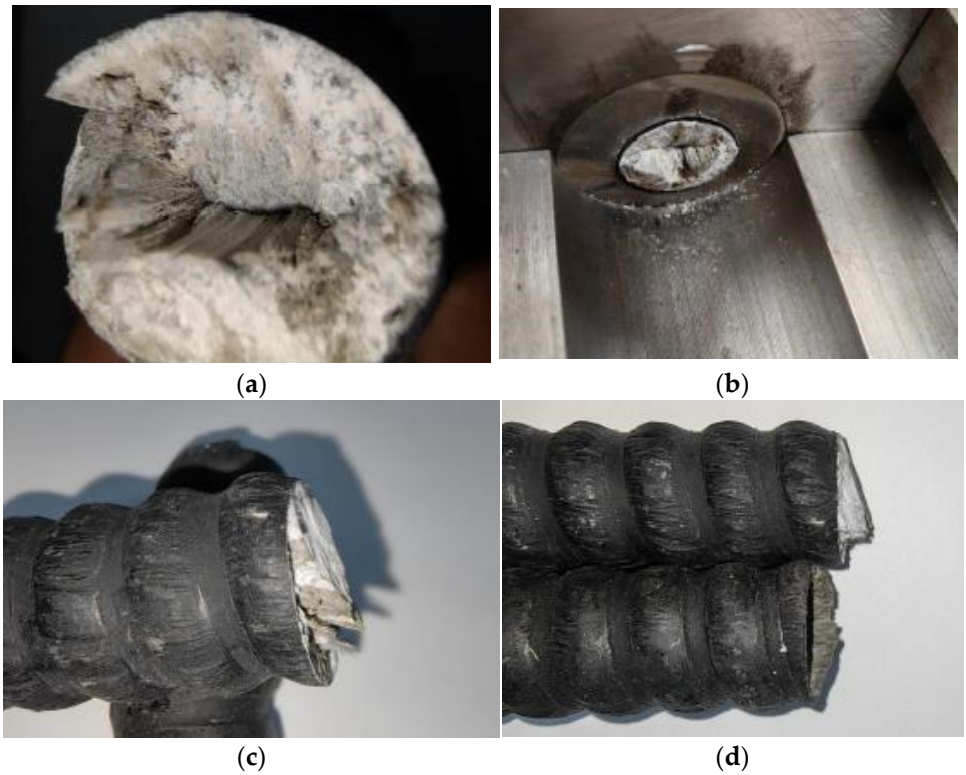

Figure 3. Macroscopic failure surfaces of BFRP bars after direct shear testing. (**a**) Smooth shear-off surface at initial failure (matrix-dominated); (**b**) Irregular surface during transition stage (onset of fiber pull-out); (**c**) Brush-like morphology after extensive fiber pull-out; (**d**) Measurement of fiber inclination angle θ on the fracture surface.

Measurements across multiple specimens showed that the inclination angles of the pulled-out fibers ranged from 11.5° to 27.1°, with an average angle of approximately 20° (Figure 3d). This failure pattern clearly demonstrates that the direct shear failure of BFRP

bars is not a simple brittle shear fracture but rather a composite process that begins with matrix shear failure and is ultimately controlled by fiber pull-out mechanisms.

3.2. Stress–Strain Curve

Figure 4 shows the corresponding vertical load–displacement curves, while Figure 5 presents the converted shear stress–strain (τ–γ) curves for all specimens. All curves exhibit a highly consistent three-stage characteristic, clearly capturing the mechanical response associated with internal damage evolution and the transition in failure modes.

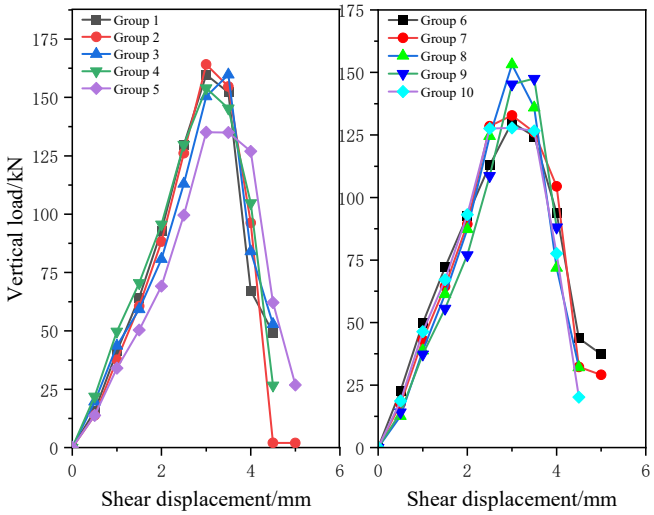

Figure 4. BFRP reinforcement vertical load-shear displacement curve relationship.

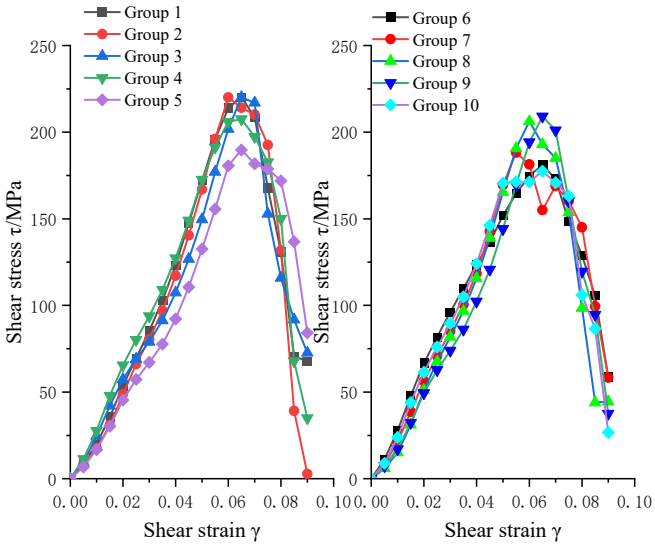

Figure 5. BFRP reinforcement shear stress–strain curve relationship.

Initial Linear Elastic Stage (Segment OA): The initial portion of the curve shows a linear shape, with shear stress (τ) directly proportional to shear strain (γ). This stage corresponds to the fully elastic response of the material (including the resin matrix, fibers, and interface). The slope of this segment represents the initial shear modulus (G_0) of the BFRP bar. During this phase, the load increases steadily, and the specimen continuously accumulates elastic strain energy.

Nonlinear Damage Softening Stage (Segment AB): After exceeding the proportional limit at point A, the curve slope gradually decreases, entering a nonlinear hardening stage. This stage marks the initiation and stable propagation of internal damage within the

material. As strain increases, microcracks begin to form in the resin matrix, accompanied by partial debonding at the fiber-matrix interface. Despite the ongoing degradation in material stiffness, shear stress continues to rise until reaching the peak point B—the peak shear strength (τ_{max})—due to the bridging effect of the fibers.

Post-peak Softening Failure Stage (After Point B): After reaching the peak strength, the curve enters the softening stage. This phase corresponds to the instantaneous propagation of macroscopic shear cracks (as indicated by the sudden drop in the load curve in Figure 6) and the subsequent fiber pull-out and shear failure process. Shear stress rapidly decreases from its peak and then enters a prolonged "plateau" or "tail" region characterized by a slow decline in load-bearing capacity. This plateau corresponds to the gradual stretching and pull-out of fibers, as illustrated in Figure 3. The stress level in this region represents the residual strength, primarily provided by the tensile performance of the fibers and interfacial friction.

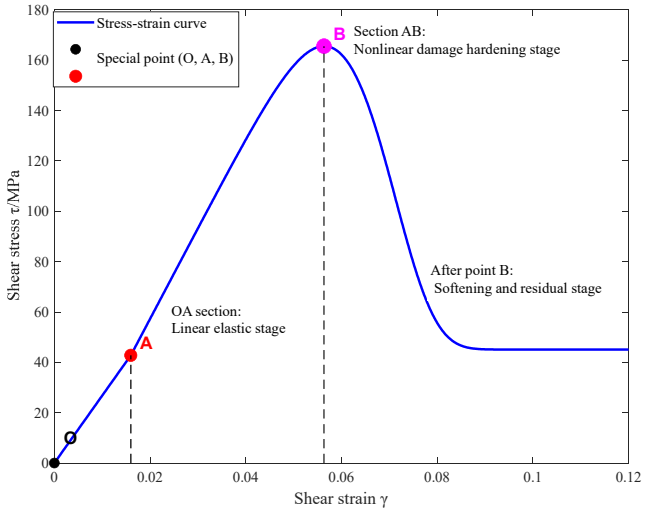

Figure 6. BFRP reinforcement shear stress–strain curve.

3.3. Analysis of Key Mechanical Indicators

Based on the experimental data, key parameters such as peak load, corresponding displacement, initial shear modulus, and shear strength for each specimen were calculated and summarized in Table 2. The shear strength was calculated using the formula, where P_{max} is the peak load and A is the cross-sectional area of the bar (370.9 mm^2). The initial shear modulus G_0 was determined from the slope of the initial linear segment of the shear stress–strain curve.

Statistical analysis of the data in Table 2 reveals the following:

The average peak shear strength of the ten specimens is 204.04 MPa, with a standard deviation of 14.79 MPa and a coefficient of variation of 7.25%. The average initial shear modulus is 3.37 GPa, with a standard deviation of 0.398 GPa and a coefficient of variation of 11.82%.

The average peak displacement (i.e., shear displacement at peak load) is 3.074 mm, with a standard deviation of 0.217 mm and a coefficient of variation of 7.06%. The variability in mechanical indicators is attributed to the inherent heterogeneity of BFRP composite materials.

The average peak shear strength of 204.04 MPa is comparable to values reported for GFRP bars under similar conditions (typically 190–210 MPa), while the residual strength plateau is more pronounced due to the higher stiffness and better interfacial bonding of basalt fibers with epoxy resin.

Table 2. BFRP reinforcement direct shear test key mechanical parameters statistical table.

Test No.	Peak Load P_{max}/kN	Peak Displacement Δ_{max}/mm	Initial Shear Modulus G_0/GPa	Shear Strength τ_{max}/MPa
1	164.490	3.185	2.799	221.744
2	164.160	2.999	2.959	221.299
3	166.890	3.325	3.423	224.979
4	158.970	3.159	3.653	214.303
5	142.590	3.165	2.884	192.222
6	134.790	3.186	3.725	181.707
7	140.160	2.732	3.213	188.946
8	154.890	3.074	3.709	208.803
9	156.360	3.251	3.372	210.785
10	137.610	2.665	3.961	185.508
Mean	152.091	3.074	3.370	204.04
Standard deviation	12.172	0.217	0.398	14.79
Coefficient of variation	8.0%	7.06%	11.82%	7.25%

3.4. Fiber Tilt Statistical Distribution and Its Influence Analysis

The fiber orientation angle θ on the shear fracture surface of BFRP bars was measured directly from high-resolution macroscopic photographs (see Figure 2) using ImageJ software. A total of 45 valid measurements were obtained, and the statistical distribution is presented in Figure 7. The inclination angle θ ranges from 11.5° to 27.1°, with a mean value of 19.7°, a standard deviation of 4.3°, and a coefficient of variation of 21.8%. The distribution of the fiber orientation angle θ ranges from 11.5° to 27.1°, with a mean value of 19.7°, a standard deviation of 4.3°, and a coefficient of variation of 21.8%. This distribution pattern directly reflects the microstructural heterogeneity of the composite material. Since the fibers within the bars are not perfectly aligned and local interfacial properties vary, the orientation of fiber pull-out during failure fluctuates within a certain range.

The fiber orientation angle θ is a key geometric parameter that closely links the macroscopic shear deformation to the axial tensile strain of the fibers. According to deformation compatibility, the relationship between the axial strain of the fibers and the macroscopic shear strain can be approximated as follows [17,18]:

$$\varepsilon_f \approx \gamma \cdot \sin\theta \cdot \cos\theta \tag{3}$$

where

θ = fiber orientation angle (degrees).

Defining a conversion coefficient, $k = \sin\theta \cdot \cos\theta$ the fiber axial strain is given by ε_f:

$$\varepsilon_f \approx k\gamma \tag{4}$$

where

k = conversion coefficient;

γ = shear strain.

For this batch of specimens, the average value of k is 0.32. Its distribution reflects the directionality and variability of the fiber bridging effect.

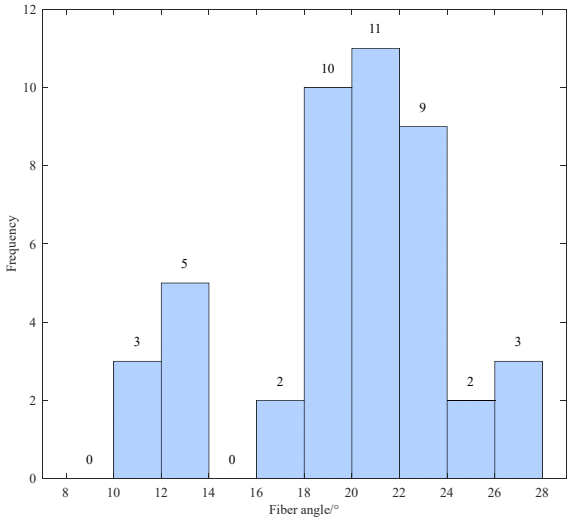

Figure 7. Fiber inclination angle θ distribution histogram.

4. Damage Constitutive Model Considering Fiber Effect

4.1. Basic Assumptions and Theoretical Basis

This paper draws upon the statistical damage theory framework established by Wang Baotian and He Liang in their studies on bolt-grout interfaces and steel-reinforced rockfill contact surfaces [16,17,19,20]. Integrating the shear failure characteristics of BFRP bars, the following fundamental assumptions are proposed:

(1) **Micro-element strength follows a Weibull distribution:** The shear plane of BFRP bars consists of a large number of randomly distributed micro-elements. The ultimate shear strength of each micro-element follows a two-parameter Weibull distribution, reflecting the inherent strength heterogeneity within the composite material.

(2) **Damage evolution adheres to a continuous statistical law:** The damage variable D represents the proportion of failed micro-elements. Its evolution is continuous and governed by strain.

(3) **Fiber bridging effect and residual strength:** During the damage process, both the intact micro-elements and the damaged regions jointly bear the load. The fiber bridging effect varies with strain, and the residual strength is provided by post-pullout friction of the fibers.

(4) **Incorporating fiber orientation angle and volume fraction:** A fiber configuration influence coefficient, k_f, is introduced to incorporate the fiber orientation angle θ and volume fraction V_f into the constitutive parameter system.

4.2. Evolutionary Laws of Damage Variables

According to statistical damage theory [17,18,20], it is assumed that the shear plane of BFRP bars consists of a large number of randomly distributed micro-elements. The ultimate shear strength of each micro-element follows a two-parameter Weibull distribution. The probability density function of the Weibull distribution can be expressed as:

$$\phi(\gamma) = \frac{m}{\gamma_0}\left(\frac{\gamma}{\gamma_0}\right)^{m-1} e^{\left[-\left(\frac{\gamma}{\gamma_0}\right)^m\right]} \tag{5}$$

where

γ = shear strain;

m = shape parameter (reflects uniformity of micro-element strength distribution);

γ_0 = scale parameter (related to average ultimate shear strain).

When the shear strain reaches $n(\gamma)$, the number of failed micro-elements can be obtained by integrating the probability density function:

$$n(\gamma) = N\int_0^{\gamma} \phi(x)dx \tag{6}$$

where

N = total number of micro-elements.

The damage variable D is defined as the proportion of failed micro-elements to the total:

$$D = \frac{n(\gamma)}{N} = \int_0^{\gamma} \phi(x)dx = 1 - e^{\left[-\left(\frac{\gamma}{\gamma_0}\right)^m\right]} \tag{7}$$

where

D = damage variable (proportion of failed micro-elements).

This equation shares a similar form with the statistical damage model for the bolt-grout interface, both reflecting the influence of the statistical distribution characteristics of the internal micro-element strength on the macroscopic damage evolution.

4.3. Constitutive Relation Construction Considering Fiber Effect

(1) Considering the influence of the fiber inclination angle θ and the volume fraction, the fiber configuration influence coefficient is defined as:

$$k_f = V_f \cdot \sin\theta \cdot \cos\theta \tag{8}$$

These factors are incorporated into the material parameters:

$$G_0 = G_{0,base} \cdot k_f;\ \eta = \eta_{base} \cdot k_f;\ \tau_{res} = \tau_{res,base} \cdot k_f \tag{9}$$

where, $G_{0,base}$, η_{base} and $\tau_{res,base}$ represent their baseline values—the unchanged reference values selected for parameter studies (such as sensitivity analysis or comparative studies on parameter variations).

(2) Based on continuum damage mechanics and statistical theory, it is assumed that the shear plane consists of a large number of randomly distributed micro-elements. The damage variable D is defined to represent the proportion of failed micro-elements (D = 0 indicates an undamaged state, D = 1 indicates complete failure). The total shear stress is jointly borne by the undamaged and damaged parts:

$$\tau(\gamma) = \tau_u(\gamma)(1 - D) + \tau_d \cdot D \tag{10}$$

where

τ_u = shear stress borne by undamaged material;
τ_d = shear stress borne by damaged material;
τ_{res} = residual shear strength;
D = damage variable.

(3) To accurately describe the aforementioned failure process, this study establishes a constitutive model based on statistical damage theory that reflects the entire shear process of BFRP bars. Assuming the shear plane consists of numerous micro-elements whose strengths follow a Weibull distribution, the damage variable D is introduced, and its evolution law is defined as:

$$D = 0 \quad \gamma \le \gamma_A \tag{11}$$

$$D = 1 - e^{\left[-\left(\frac{\gamma-\gamma_A}{\gamma_0}\right)^m\right]} \quad \gamma > \gamma_A \tag{12}$$

(4) Unified Constitutive Equations

Comprehensively considering the linear elastic response, fiber bridging effect, and residual strength, the unified constitutive equations are established as follows:

$$\tau(\gamma) = G_0\gamma \quad \gamma \le \gamma_A \text{ (Elastic Stage)} \tag{13}$$

$$\tau(\gamma) = [G_0\gamma + \eta(\gamma-\gamma_A)]e^{\left[-\left(\frac{\gamma-\gamma_A}{\gamma_0}\right)^m\right]} + \tau_{res}\{1 - e^{\left[-\left(\frac{\gamma-\gamma_A}{\gamma_0}\right)^m\right]}\} \ \gamma > \gamma_A \text{ (Damage and Softening Stage)} \tag{14}$$

where

G_0 = initial shear modulus (reflects matrix-dominated elastic stiffness);

η = fiber bridging stiffness coefficient (reflects fiber contribution to stiffness enhancement);

τ_{res} = residual shear strength (reflects frictional resistance after fiber pull-out).

4.4. Parameter Calibration and Model Verification

The model parameters were fitted using the experimental data, with the results presented in Table 3. A least squares method was applied to fit the 10 sets of test curves. Except for specimen No. 2 (which may have been affected by an anomaly or defect), the coefficient of determination R^2 for the remaining specimens exceeded 0.98, demonstrating the model's strong applicability. The fitted parameters possess clear physical meanings:

The m values ranged from 3.84 to 9.91, corresponding to material uniformity (strength dispersion). An inverse correlation was observed between m and α, confirming that earlier damage initiation corresponds to greater material brittleness.

The constitutive model parameters obtained through fitting are as follows: G_0 = 2679.0 MPa, α = 0.0160, η = 922.6 MPa, m = 8.23, γ_0 = 0.0698, τ_{res} = 45.1 MPa.

Table 3. Statistical damage model parameters fitting results of BFRP reinforcement.

Number	G_0/MPa	γ_A	η/MPa	m	γ_0	τ_{res}/MPa	R^2
1	2911.1	0.0268	1000.0	9.91	0.0502	64.5	0.9878
2	2010.1	0.0037	552.8	8.33	0.0763	67.2	0.5808
3	2204.4	0.0067	492.2	7.35	0.0723	94.0	0.7962
4	2775.5	0.0143	845.2	9.14	0.0674	17.4	0.9872
5	1797.9	0.0021	525.1	8.03	0.0830	77.1	0.8143
6	2525.0	0.0010	596.0	8.58	0.0783	53.5	0.9852
7	2806.3	0.0279	1000.0	3.84	0.0554	10.0	0.9812
8	2769.3	0.0266	1000.0	8.62	0.0500	37.6	0.9840
9	2632.3	0.0340	1000.0	6.56	0.0460	43.8	0.9757
10	2333.4	0.0080	1000.0	8.14	0.0734	10.0	0.9814

Note: Given that specimen No. 2 may have exhibited behavior significantly deviating from the trend due to unobserved initial defects, it was excluded when calculating the average model parameters and during subsequent correlation analysis to ensure the generality of the conclusions.

A comparison between the experimental results and the curves simulated by the damage constitutive model (as shown in Figure 8) indicates that, although the model curves show some numerical deviation from the experimental data, they effectively capture the shear characteristics of the BFRP bar fracture surfaces.

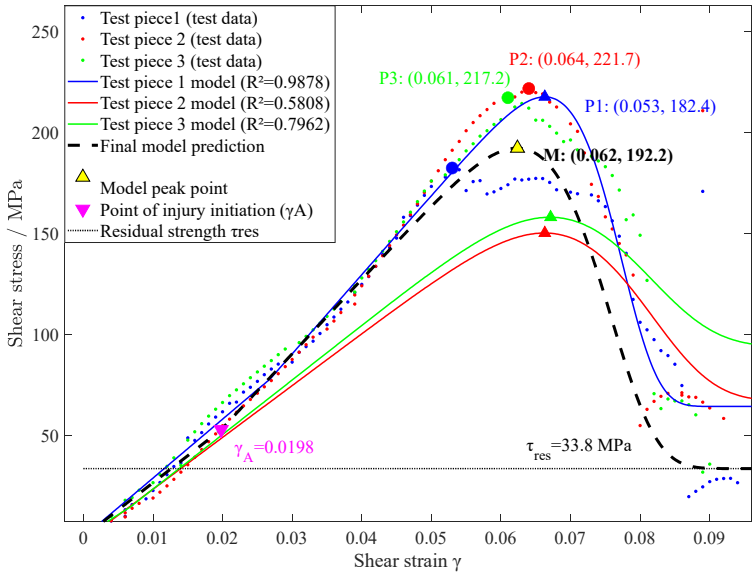

Figure 8. Comparison of Stress–Strain Curves of BFRP Bars in Shear Tests with Statistical Damage Model.

4.5. Sensitivity Analysis of Parameters

The sensitivity analysis was conducted using a parameter perturbation method: each parameter was varied by ±20% while keeping others constant, and the resulting changes in the stress–strain curve were quantified.

Through variations in different parameter values (see Figure 9), it was found that the shape parameter m reflects the degree of dispersion in the strength of micro-elements and primarily affects the post-peak softening stage. A smaller m indicates a more scattered strength distribution, where damage develops gradually, resulting in a slower softening process. Conversely, a larger m indicates concentrated strength, where once damage initiates, it propagates rapidly, manifesting as brittle behavior.

Based on the sensitivity analysis of each parameter in the statistical damage model for BFRP bars, the following conclusions can be drawn:

The Weibull shape parameter m primarily controls the post-peak softening behavior. A larger m leads to more concentrated damage evolution, resulting in brittle fracture characteristics of the material. The scale parameter γ_0 influences the position of the peak strain and the softening path. A larger value indicates better material ductility.

The fiber bridging stiffness coefficient η significantly enhances the nonlinear hardening stage before the peak, improving the peak load-bearing capacity. The residual shear strength τ_{res} almost independently determines the height of the post-peak residual stress plateau, reflecting the interfacial friction and interlocking effects after fiber pull-out.

These four parameters collectively characterize the constitutive behavior of BFRP bars throughout the entire shear process, addressing the aspects of damage evolution, toughness characteristics, stiffness enhancement, and residual load-bearing capacity.

The correlation analysis among parameters (Table 4) reveals their intrinsic physical relationships, with the following particularly significant findings:

(1) **Strong negative correlation between γ_A and γ_0 ($r = -0.983$):** This indicates that earlier damage initiation corresponds to a smaller characteristic damage strain γ_0, resulting in more pronounced brittle behavior in the material.

(2) **Strong negative correlation between η and γ_0 ($r = -0.806$):** This suggests that a stronger fiber bridging effect leads to more concentrated damage development.

(3) **Positive correlation of G_0 with γ_A and η ($r > 0.75$):** Specimens with higher initial stiffness generally exhibit a higher damage threshold and more significant fiber bridging contributions. This result reflects the interconnectedness of overall material performance.

(4) **Negative correlation between τ_{res} and η ($r = -0.737$):** Specimens with greater fiber bridging stiffness contributions tend to show a trend of reduced residual strength. This may imply a potential trade-off between interfacial designs aimed at enhancing pre-peak bridging stiffness (η) and those focused on maximizing post-pullout friction (τ_{res}).

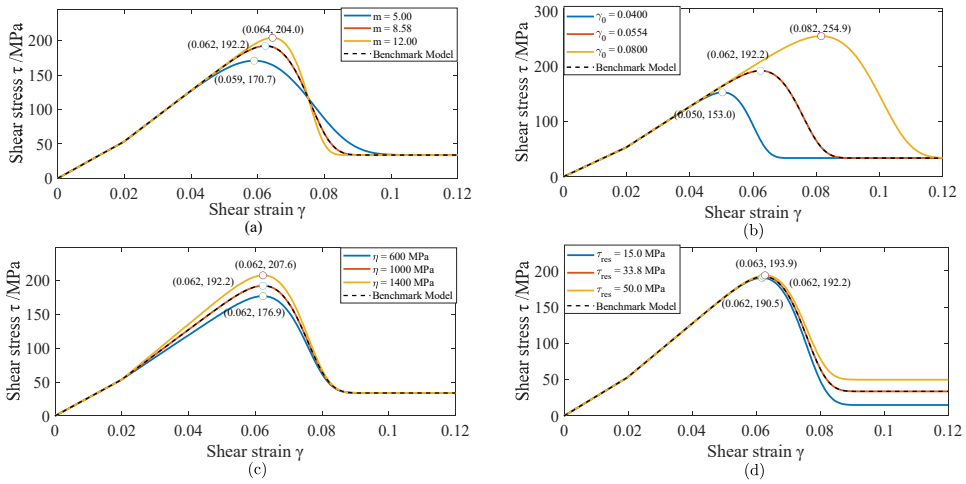

Figure 9. BFRP reinforcement statistical damage model parameter sensitivity analysis (**a**) Weibull shape parameter m sensitivity analysis; (**b**) Sensitivity analysis of scale parameter γ_0; (**c**) Sensitivity analysis of fiber bridging stiffness coefficient η; (**d**) Residual shear strength τ_{res} sensitivity analysis.

Table 4. Parameter correlation analysis.

	G_0	γ_A	η	m	γ_0	τ_{res}
G_0	1.000	0.759	0.776	−0.041	−0.790	−0.547
γ_A	0.759	1.000	0.826	−0.316	−0.983	−0.385
η	0.776	0.826	1.000	−0.156	−0.806	−0.737
m	−0.041	−0.316	−0.156	1.000	0.201	0.294
γ_0	−0.790	−0.983	−0.806	0.201	1.000	0.315
τ_{res}	−0.547	−0.385	−0.737	0.294	0.315	1.000

4.6. Macro-Micro Correspondence of Damage Evolution and Failure Process

As shown in Figure 10a, the damage evolution curves of all specimens with high goodness of fit ($R^2 \geq 0.85$) exhibit a typical "*S*"-shaped growth trend, which aligns with the fundamental characteristics of the cumulative probability function of the Weibull distribution. The curve can be divided into three key stages:

(1) **Damage Incubation and Slow Initiation Stage ($D < 0.2$):** The initial segment of the curve is relatively flat, with a slow increase in the *D*-value. This corresponds to the initial failure of randomly distributed weak micro-elements within the material, where damage has not yet formed effective connectivity.

(2) **Damage Accelerated Propagation Stage ($0.2 < D < 0.8$):** The slope of the curve increases significantly, and the *D*-value rises rapidly. This stage corresponds to the chain effect of micro-element failures and the formation of localized shear bands, representing the primary phase of macroscopic mechanical property degradation (e.g., stiffness reduction).

(3) **Damage Saturation and Stabilization Stage ($D > 0.8$):** The curve gradually flattens and approaches $D = 1$. This indicates that the macroscopic shear plane has essentially fully developed, and the material's load-bearing capacity is predominantly sustained by residual mechanisms (fiber bridging).

Figure 10b clearly demonstrates the decisive role of the shape parameter m in determining the damage evolution path. By comparing theoretical curves for low (m = 3.84), medium (m = 8.58), high (m = 9.91), and average (m = 7.85) values, the following conclusions can be drawn:

(1) **The m-value controls the steepness of the curve:** A larger m-value results in a steeper curve during the damage accelerated propagation stage (D = 0.2–0.8), indicating that damage rapidly transitions from initiation to saturation within a narrow strain range. This corresponds to a highly concentrated distribution of micro-element strengths within the material, with fewer micro-defects. Once critical conditions are met, damage propagates swiftly, manifesting as more pronounced brittle behavior macroscopically.

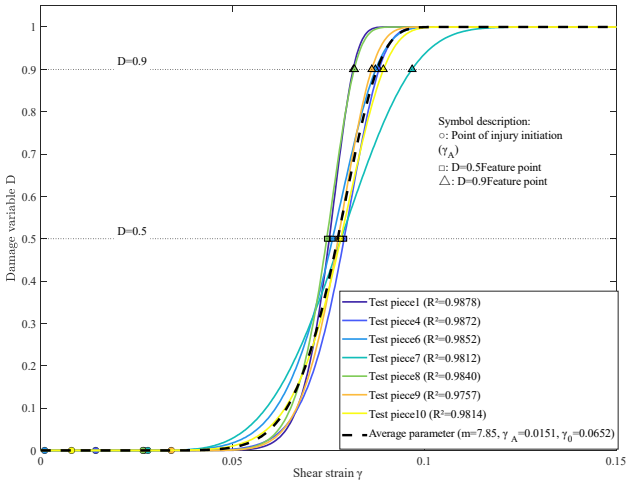

(**a**)

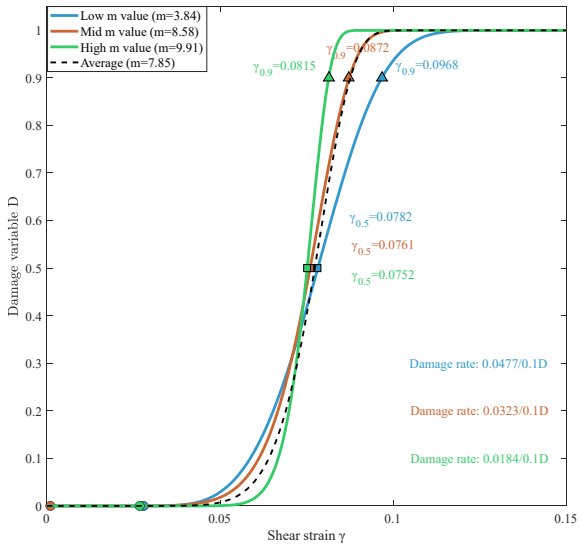

(**b**)

Figure 10. Damage variable D evolution law with strain of BFRP fiber statistical damage model (**a**) Damage evolution curve of high-fidelity specimen ($R^2 \geq 0.85$) (**b**) Comparison of damage evolution at different m values.

Conversely, a smaller m-value yields a flatter curve, prolonging the damage evolution process and endowing the material with greater ductility or pseudo-plasticity.

(2) **The m-value determines the damage propagation rate:** Quantitative calculations of the average damage rate ($\Delta D/\Delta\gamma$) during the transition from D = 0.5 to D = 0.9 for different m-values reveal that, from the perspective of damage evolution dynamics, the damage rate is positively correlated with m. This further corroborates the earlier mechanical analysis conclusion that "reducing m can delay interface softening and stiffness degradation".

(3) **Relationship between m-value and macroscopic failure mode:** Rapid damage evolution associated with high m-values correlates with the sharp post-peak drop in shear stress observed macroscopically (indicative of brittle failure). In contrast, slow damage evolution associated with low m-values corresponds to a broad, gentle softening stage and a prolonged residual plateau (indicative of ductile failure). This finding provides a perfect explanation for the differences in post-peak shear stress–strain curve shapes observed in Figure 9 for different m-values.

4.7. Model Comparison and Applicability Discussion

To validate the rationality and advancement of the proposed model, the predicted peak shear strengths are compared with both the experimental results reported by Protchenko [11] for BFRP and HFRP bars and the empirical shear strength models from Protchenko [11] (Equation (15)) and ACI [10] (Equation (16)). Using the average test parameters obtained in this study (V_f = 70%, f_{fu} = 1000 MPa, d = 22 mm), the predicted values from the selected models were calculated and are summarized in Table 5.

$$\tau_u = 0.2 f_{fu} \tag{15}$$

$$\tau_u = k \cdot f_{fu} \tag{16}$$

where

f_{fu} = ultimate tensile strength of the FRP bar (MPa);

k = empirical coefficient (typically 0.2–0.4, depending on fiber type and interfacial bonding).

Table 5. Model comparison results.

Model	Predict τ_{max} (MPa)	Experiment τ_{max} (MPa)	Relative Deviation (%)
Protchenko	206.2	204.0	+1.1
ACI	200	204.0	−1.98
The model of this paper	203.2	204.0	–0.4

Protchenko [11] conducted double-shear tests on BFRP and hybrid basalt/carbon FRP (HFRP) bars with diameters ranging from 6 mm to 18 mm, reporting average shear strengths of 170–210 MPa for BFRP bars and 202–229 MPa for HFRP bars. The average shear strength of BFRP bars (d = 22 mm) obtained in this study (204.04 MPa) is in excellent agreement with the range reported by Protchenko [11], confirming the reliability of the experimental dataset.

Beyond shear performance, BFRP bars offer distinct material advantages over conventional reinforcement and other FRP types. With a density of only 2.0 g/cm^3, BFRP achieves a strength-to-weight ratio approximately 20 times higher than steel, while providing superior corrosion resistance and competitive material cost. Compared to GFRP, BFRP exhibits higher stiffness and better alkali resistance; compared to CFRP, BFRP presents

a more economical solution with lower embodied energy. These characteristics position BFRP as a balanced and sustainable alternative for modern infrastructure.

Compared to traditional empirical formulas that only predict peak strength, the statistical damage constitutive model established in this study represents a theoretical advancement from "single-point strength prediction" to "full-process behavior description". Traditional models are essentially phenomenological simplifications based on macroscopic test data, often neglecting meso-scale physical mechanisms such as fiber bridging, residual strength, and progressive damage evolution [21].

In contrast, the proposed model is grounded in statistical damage theory. By introducing the Weibull distribution to describe micro-element strength and defining the fiber bridging stiffness coefficient η and residual strength τ_{res}, the model successfully integrates the complete shear process—from matrix elasticity, damage-induced hardening, peak softening, to fiber pull-out residual behavior—with all parameters possessing clear physical significance. This not only ensures excellent fitting accuracy (with R^2 generally exceeding 0.98) but also provides a reliable theoretical tool for refined analysis and performance-based design of BFRP bars in applications such as reinforced soil and anchoring engineering.

Scope and Limitations:

The model is developed based on quasi-static (0.5 mm/s) room-temperature direct shear tests. For applications involving different strain rates, temperatures, or multiaxial stress states (e.g., confining pressure, coupled axial tension), the parameters (G_0, η, τ_{res}) may need to be calibrated as functions of strain rate and temperature. Long-term effects such as creep and stress relaxation are not considered and should be addressed in future durability studies.

5. Conclusions

1. The direct shear failure of BFRP bars exhibits a clear three-stage progressive process: initial failure triggered by shear in the resin matrix, peak load-bearing capacity maintained by fiber bridging, and eventual fiber pull-out contributing to residual strength. The average fiber inclination angle of approximately 20° is a key geometric feature enabling this bridging effect. This three-stage behavior is comprehensively captured by the statistical damage model developed in this study, with the damage initiation strain γ_A and the shape parameter m respectively governing the transition from the first to the second stage and the rate of post-peak softening.
2. The established statistical damage constitutive model successfully describes the full-range mechanical behavior of BFRP bars under shear. The model parameters have clear physical meanings: G_0 and γ_A characterize the elastic properties of the material; η and τ_{res} represent the reinforcing effect of fibers; m and γ_0 govern the statistical evolution of damage.
3. The parameter m is a key factor controlling post-peak performance. Reducing the m value significantly slows the rate of damage accumulation and propagation, resulting in a more gradual stress-softening curve and improved ductility. This insight provides theoretical guidance for material optimization: for instance, improving manufacturing uniformity (e.g., better fiber dispersion and reduced voids) to lower m can enhance the ductility of BFRP bars, making them more suitable for seismic-resistant designs where post-peak energy dissipation is critical.
4. Parameter sensitivity analysis and correlation analysis confirm the physical self-consistency of the model. The strong negative correlation between γ_A and γ_0 ($r = -0.983$) links early damage initiation to brittle characteristics; the negative correlation between η and τ_{res} ($r = -0.737$) suggests a potential trade-off between pre-peak bridging stiffness and post-pullout frictional resistance. These findings offer important

references for performance-oriented design of BFRP bars, enabling engineers to tailor material compositions and processes to achieve desired shear responses in applications such as reinforced soil structures, anchor systems, and composite reinforcements.

5. Future work should include SEM observations to directly visualize micro-crack propagation, fiber-matrix debonding, and the fiber pull-out process, thereby providing direct microstructural validation of the proposed damage mechanisms.
6. Moreover, BFRP bars are produced from abundant basalt rock with lower energy consumption than steel or carbon fibers, resulting in reduced carbon footprint and life-cycle cost. Their corrosion resistance eliminates the need for cathodic protection and reduces maintenance, further enhancing their sustainability profile.

Author Contributions: Conceptualization: F.L.; Methodology: F.L. and P.Z.; Software: P.Z.; Validation: P.Z.; Formal Analysis: F.L., P.Z. and J.G.; Investigation: P.Z.; Resources: F.L. and Y.W.; Data Curation: F.L. and Y.W.; Writing—Original Draft Preparation: F.L. and P.Z.; Writing—Review and Editing: F.L., P.Z., J.G. and Y.W.; Visualization: F.L.; Supervision: F.L., J.G. and Y.W.; Project Administration: F.L. and J.G.; Funding Acquisition: F.L. and J.G. All authors have read and agreed to the published version of the manuscript.

Funding: This research was funded by the National Natural Science Foundation of China, grant number 52104082.

Data Availability Statement: The data are available from the corresponding author upon request.

Conflicts of Interest: The authors declare no conflict of interest.

References

1. Wang, F.; Zhang, X.; Chen, L.; Li, J.; Shao, J. On Finite Element Analysis on Stress Profiles around Broken Fibers in Unidirectional Composites. *J. Southwest China Norm. Univ. Nat. Sci. Ed.* **2013**, *38*, 106–110.
2. Liyue, M.; Liu, J.; Xiuli, D. Comparative analysis of seismic performance of concrete shear walls reinforced with steel bars and BFRP bars. *J. Vib. Eng.* **2025**, *38*, 2160–2171.
3. Sharif, H.H.; Mahmood, A.D. Shear performance of sustainable BFRP-reinforced concrete beams with stirrup incorporating recycled plastic aggregates: Experimental and analytical Investigations. *Constr. Build. Mater.* **2025**, *503*, 144530. [CrossRef]
4. Liao, J.; Di, B.; Zheng, Y.; Chen, T.-G.; Zeng, J.-J.; Zhuge, Y. Shear behavior of FRP-reinforced concrete beams with basalt FRP grids as shear Reinforcements. *Eng. Struct.* **2025**, *339*, 120696. [CrossRef]
5. Feng, J.; Chen, J.; Wang, D. Research on Direct Shear Tests and Calculation Methods for BFRP Anchor Rods Reinforcing Rock Joint Surfaces. *Rock Mech. Rock Eng.* **2025**, *58*, 6637–6652. [CrossRef]
6. Al Hawarneh, A.; Al Martini, S.; Sabouni, R.; Al Mzayyen, N.; Alam, S. Shear behavior of concrete beams reinforced with basalt FRP rebars and incorporating recycled Aggregates. *Structures* **2025**, *78*, 109250. [CrossRef]
7. Xie, J.; Wang, X.; Ding, L.; Peng, Z.; Liu, X.; Mao, W.; Wu, Z. Shear behavior of BFRP Anchor-jointed rock mass considering inclination angle and pre-Tension. *Constr. Build. Mater.* **2024**, *447*, 138157. [CrossRef]
8. Kampmann, R.; Tang, Y.; Telikapalli, S.; Hoque, S.S. *BFRP Rebar Characterization and Performance: Testing Protocol and Material Specifications for Basalt Fiber Reinforced Polymer Bars*; Florida Department of Transportation: Tallahassee, FL, USA, 2022.
9. Yin, L.; Zhu, Y.; Xie, Q.; Cai, X. Strength degradation and uncertainty evaluation of heated GFRP and BFRP rebars with or without seawater Sea-sand mortar Cover. *J. Build. Eng.* **2025**, *115*, 114470. [CrossRef]
10. ACI Committee 440. *Guide for the Design and Construction of Structural Concrete Reinforced with FRP Bars (ACI 440.1R-23)*; American Concrete Institute: Farmington Hills, MI, USA, 2023.
11. Protchenko, K.; Zayoud, F.; Urbański, M.; Szmigiera, E. Tensile and shear testing of basalt fiber reinforced polymer (BFRP) and hybrid basalt/carbon fiber reinforced polymer (HFRP) bars. *Materials* **2020**, *13*, 5839. [CrossRef] [PubMed]
12. Wang, Z.; Zhang, W.; Duan, J.; Zhang, X.; Zhao, J. Experimental study on shear properties of FRP bars. *Mater. Rep.* 2025, *ahead of print*. Available online: https://link.cnki.net/urlid/50.1078.TB.20250829.1003.016 (accessed on 13 February 2026).
13. Lin, H.; Qu, H.; Yang, J.; Li, X.; Xu, H.; Feng, P. Investigation on the relationship between the transverse shear strength and tensile strength of FRP bars. *Acta Mater. Compos. Sin.* 2025, *ahead of print*. [CrossRef]
14. Huang, M.; Zhou, Z.; Ou, J. Nonlinear full-range analysis of load transfer fixed segment of tensile anchors. *Chin. J. Mech. Eng.* **2014**, *33*, 2190–2199.

15. Guo, H. Discussion on the "Constitutive Model of Non-Penetrating Fractured Rock Mass Based on Coupling of Macro- and Microp damages. *Rock Soil Mech.* **2018**, *39*, 1923–1924.
16. He, L.; Li, G.; Li, X. Shear characteristics of the contact surface between ribbed bars and rockfill materials. *J. Hohai Univ. Nat. Sci.* **2019**, *47*, 138–143.
17. Ren, F.F.; Yang, Z.J.; Chen, J.F.; Chen, W.W. An analytical analysis of the full-range behaviour of grouted rockbolts based on a tri-linear bond-slip model. *Constr. Build. Mater.* **2010**, *24*, 361–370. [CrossRef]
18. Cai, Y.; Esaki, T.; Jiang, Y. An analytical model to predict axial load in grouted rock bolt for soft rock tunnelling. *Tunn. Undergr. Space Technol.* **2004**, *19*, 607–618. [CrossRef]
19. Luo, L.; Gao, Z.; Hu, L. Research on compressive constitutive models and seismic performance of common brick masonry structures with different masonry methods. *Eng. Constr.* 2025, *ahead of print*. Available online: https://link.cnki.net/urlid/43.1465.TU.20251208.1725.002 (accessed on 13 February 2026).
20. Wang, B.; Zhou, B.; Zhou, T. Analysis of the whole course for the force transferring mechanism in anchor bar based on statistical damage constitutive theory. *J. Hohai Univ. Nat. Sci.* **2018**, *46*, 314–320.
21. Xia, H.; Zhou, G.; Shang, X. Statistical damage softening constitutive model of soil—Structure interface based on Weibull random distribution. *J. China Univ. Min. Technol.* **2007**, *36*, 734–737.

Disclaimer/Publisher's Note: The statements, opinions and data contained in all publications are solely those of the individual author(s) and contributor(s) and not of MDPI and/or the editor(s). MDPI and/or the editor(s) disclaim responsibility for any injury to people or property resulting from any ideas, methods, instructions or products referred to in the content.